AERODYNAMIC DESIGN AND WIND TUNNEL TEST OF A LAMINAR WING WITH SPLIT FLAP FOR A FUEL CELL POWERED AIRCRAFT

J. Frey[1], F. Sell[1], R. Gillespy[2], H. Pfifer[1]
[1]TU Dresden, Chair of Flight Mechanics and Control, 01062 Dresden, Germany
[2]University of Nevada Reno, Department of Mechanical Engineering, 89557 Reno, USA

Abstract

This paper presents a wing design for the APUS i-2 concept hydrogen fuel cell aircraft that meets design requirements for hydrogen storage, lift and drag characteristics and manoeuvrability. Airfoil polars and lift distribution calculations were produced on a split-flap wing using XFOIL and Athena Vortex Lattice (AVL) software. Computer results were used to modify the wing design until an optimal airfoil shape was developed for both cruise and landing conditions. A model of the airfoil design was then manufactured for wind tunnel testing at TU Dresden to produce experimental lift and drag results, which were later compared to the theoretical data. The results collected throughout the experimental campaigns were extrapolated to a finite wing using numerical lifting line methods to fully model the final wing design's aerodynamic behaviour on the i-2 aircraft. Finally, the aircraft's manoeuvrability with the given ailerons and induced drag reduction efforts were investigated.

1. INTRODUCTION

To achieve climate neutrality, the European Green Deal set the goal to reduce transport emissions by 90% from 1990 to 2050 [1]. The aviation sector has significant potential to contribute to this emission reduction by using renewable energies and developing electric propulsion in aircraft. A notable barrier to electric aircraft, however, is the limited energy density of batteries [2]. Hydrogen may be a higher-density energy solution that provides electrical power to an aircraft through chemical reactions in a fuel cell [3].

Recent developments in implementing hydrogen power technology in general aviation incorporate both fuel cells and batteries for buffering power peaks in electric propulsion methods [4, 5]. Advancements have significant potential for transport emissions reductions, as green hydrogen can be generated from water and electricity, and water is hydrogen power's only material emission. Despite its high energy density, however, hydrogen under standard conditions has a very low mass density, so it can only be stored in sufficient quantities as a liquid in cryogenic tanks or as a gas under high pressure [3].

For preliminary wing design classical methods are still in use that incorporate potential theory models because they do not require much computational power. For airfoil performance estimations, codes like XFOIL have proven their validity compared to high fidelity tools for even lower Reynolds numbers [6]. In this publication, its extension to split flaps is demonstrated. For lift distributions, lifting line theory is universally valid, and therefore vortex lattice codes are still widely used for induces drag computation [7].

The APUS i-2 is a concept aircraft designed to contribute to emission reductions in the aviation sector using hydrogen fuel cell technology, but a major obstacle to overcome is the plane's wing design logistics. Developing an airfoil that meets the design criteria for the i-2 will demonstrate continued development of clean energy aircraft, as the implementation of a zero-emission power system has ground-breaking potential for the aviation field.

Computer-based simulations were used to converge to a suitable airfoil in cruise and high lift configurations. Experimental validation using TU Dresden's wind tunnel supported the final theoretical design's aerodynamic capability. A full three-dimensional wing's maximum lift, aileron effectiveness with the final airfoil design and potential for induced drag reduction were estimated. These contributions to the development of the i-2 concerning aerodynamics may further progress the i-2 as physical production and a maiden flight are planned.

2. PROBLEM FORUMLATION

2.1. Design Requirements

The most distinguishing feature of the airplane's design is the storage of over 20 kg of gaseous hydrogen at up to 300 bars of pressure in tubular tanks that simultaneously operate as wing spars (see FIG 1). Preliminary performance estimations completed by the leading project partner resulted in a defined wing geometry. This incorporates a large rectangular middle section spanning 9 meters and tapered outer double-trapezoids bearing the ailerons with a 5° dihedral. The entire wing uses the same airfoil with no twist to contain the cylindrical tank tubes.

The i-2 aircraft wing has specific design criteria in the form of wing dimensions and performance specifications (see table 1). These result in a cruise lift coefficient $c_{L,cruise}$ of 0.54 and a maximum lift coefficient $c_{L,max}$ of at least 1.63.

The four major requirements in which the design decisions investigated in this paper are:

- Sufficient hydrogen storage volume
- Reduction of both parasitic and induced drag
- Maximum lift in slow flight situations

doi: 10.25967/570209

– Roll moments and roll rates produced by ailerons for manoeuvrability

A relatively thick airfoil is desired with strong performance at low c_L close to the wing tips to meet the storage volume and cruise lift coefficient requirements. Because of the difference between cruise and stall speed, high lift devices must also be considered to ensure the necessary maximum lift coefficient is reached. As the planform leaves limited space for the tapered outer wings that bear the ailerons, particular attention should be paid to the agility around the roll-axis.

FIG 1. Concept APUS i-2 aircraft design © apus-zero.de

TAB 1. APUS i-2 known planform variables and flight specifications[1]

Wingspan	12.6 m	**MTOW**	1800 kg
Surface area	18.0 m²	**Cruise speed at 8500 feet**	120 kts
Aspect ratio	8.82	**Stall speed at sea level**	61 kts
Root chord	1.509 m	**Range**	500 NM

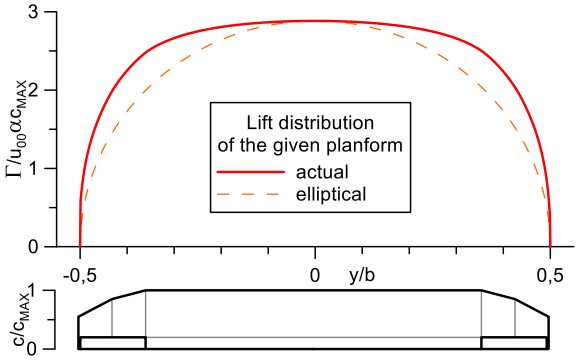

FIG 2. Planform lift distribution (top) compared to an elliptical (dashed) and planform shape (bottom); the lift is the circulation normalized with the free stream velocity angle of attack and maximum chord length.

The induced drag of the wing is an issue because of the comparatively high span loading. The non-elliptical planform results in a more full-bodied lift distribution (FIG 2) an induced drag of 3.5% above that of the elliptical distribution. Due to the weak taper and strong gradients close to the tips, it is likely that induced drag can be significantly reduced by wing tip devices, such as winglets.

2.2. Methodology

2.2.1. Theory

Airfoil performance estimations, both under wind-tunnel and free flight conditions, were done in XFOIL as well as aileron effectiveness calculations on the airfoil level. XFOIL is a well-known and easy to use tool for calculation of airfoil properties [8]. It is based on the zone approach consisting of a potential theory flow for the far field which delivers the pressure distribution and a boundary layer model to calculate wall shear and displacement thickness. The displacement thickness is then added to the contour which results in another pressure distribution. Because the boundary layer solution is dependent from the pressure gradients, the problem musts be solved by iteration.

An in-house lifting line code was applied for calculation of the induced drag, the maximum lift of the finite wing with partial flaps and rolling manoeuvres. The code is based on a discretized formulation of the classical Prandtl lifting line theory.

According to the Kutta-Joukowski theorem, the lift of a wing is a function of the spanwise circulation distribution of the bound vortex:

$$L = \rho_\infty u_\infty \int_{-b/2}^{b/2} \Gamma(y)\,dy \tag{1}$$

The local bound vortex strength is coupled with the lift coefficient, which is dependent on the effective angle of attack.

$$\Gamma(y) = c_L(y)\frac{c(y)u_\infty}{2} \tag{2}$$

$$c_L = f(\alpha_{EFF}) \tag{3}$$

The effective α differs from the geometrical by the induced angle of attack.

$$\alpha_{EFF} = \alpha_{GEO} - \alpha_i = \alpha_{GEO} - \frac{w_i}{u_\infty} \tag{4}$$

Induced flow angles are caused by the downwind that originates from the trailing vortices, as described in the lifting line theory. These form a continuous vortex sheet with the strength $d\Gamma/dy$, which is the spanwise gradient of the lifting vortex. The flow angle caused by a half infinite vortex sheet at a given spanwise position y_P is:

$$\alpha_i(y_P) = \frac{1}{4\pi u_\infty}\lim_{\varepsilon\to 0}\left(\int_{-b/2}^{y_P-\varepsilon}\frac{d\Gamma}{dy}\frac{1}{y_P-y}\,dy + \int_{y_P-\varepsilon}^{b/2}\frac{d\Gamma}{dy}\frac{1}{y_P-y}\,dy\right) \tag{5}$$

[1] These data refer to the initial specification of the project that was the basis for aerodynamic considerations.

and is therefore a function of the lift distribution again.

For a numerical solution, the system of continuous bound vortex and trailing vortex sheet can be substituted by a number of horseshoe vortices or a step function for Γ (FIG 3) with finite vortices $\Delta\Gamma$ trailing from each step, respectively.

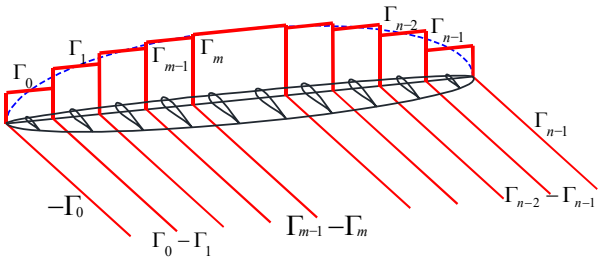

FIG 3. Lifting line model with a stepwise function for the circulation distribution

The induced flow angle acting on the middle of each spanwise section can then be written as follows:

(6) $$\alpha_i(y_P) = \frac{1}{4\pi u_\infty}\sum_{i=0}^{n}\Delta\Gamma_i\frac{1}{y_P - y_i}$$

The resulting system of equations can be solved using a standard method in the linear regime; for nonlinear c_L-α-curves, an iterative solution can be obtained by feeding the resulting flow angles into the circulation distribution again and again. Damping must be applied to avoid numerical instability

(7) $$\alpha_{EFF,t+1} = k\alpha_{EFF,t} + (1-k)(\alpha_{GEO} - \alpha_{i,t+1})$$

where typical damping factors are between $k=0.95$ and $k=0.995$.

Athena Vortex Lattice (AVL) was used for detailed induced drag calculations concerning the effect of wing tip devices such as winglets [9]. AVL is a program for calculation of lift distributions using the vortex lattice method, which is an extension of the lifting line theory described above to more than one lifting line based on horseshoe vortices (FIG 4). This way, low aspect ratio wings and sweep can be handled more properly. Moreover, AVL allows dihedral which is not implemented in the in-house code. On the other hand, vortex lattice methods cannot handle nonlinear lift curves.

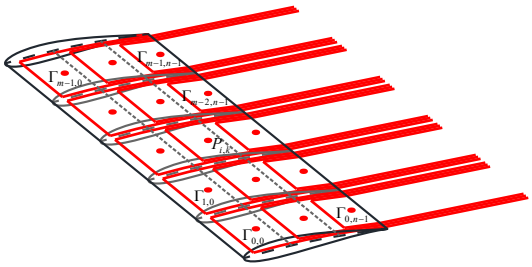

FIG 4. Vortex lattice model consisting of a chordwise and spanwise arrangement of horseshoe vortices; their strength is determined by the condition that all surface-normal velocities vanish in the control points (P).

2.2.2. Experimental Setup

TU Dresden operates a low-speed Göttingen-type wind tunnel with a closed circuit but an open test section (FIG 5). The tunnel has a circular nozzle with a 3-meter diameter and provides flow velocities of up to 40 m/s. Its contraction ratio is 7:1, leading to a free stream turbulence below 0.5%.

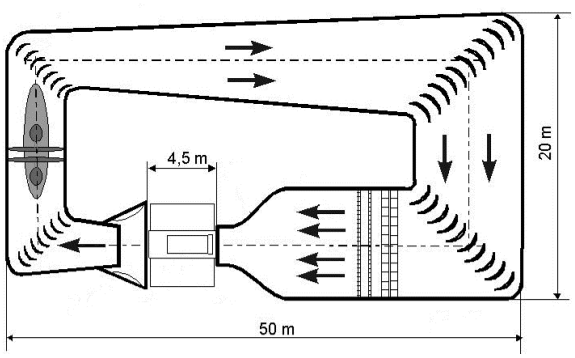

FIG 5. Low speed wind tunnel of TU Dresden

The wind tunnel model is a rectangular wing segment installed between two circular end plates (FIG 6, 7). The model has a 0.6-meter chord length and a 1.2-meter span, which is reasonable concerning test section blockage. The model comprises a split flap that can remotely be deflected midstream by an electro-mechanical drive unit. The wing box was CNC-machined out of particleboard, while the trailing edge section and flap are milled out of Necuron®, a model-making plastic material. The model is equipped with 81 pressure taps in total, with 49 in a staggered pattern near the centre line and 32 in two rows close to the endplates to measure spanwise gradients. Integrating the pressure distribution on the surface determines lift, pitching moment, and flap moment. A pitot rake is used to detect wake momentum loss for calculating profile drag. A pressure scanning system with up to 116 channels is used to collect the data.

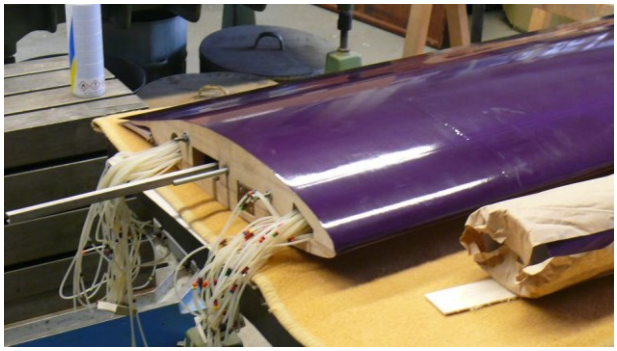

FIG 6. Root of the wing model with pressure hoses

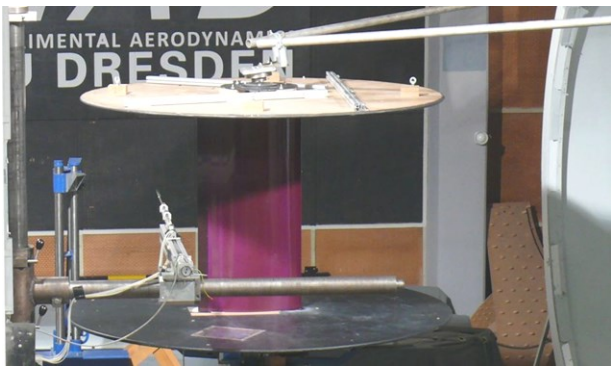

FIG 7. Wing model installed into the wind tunnel's test section

2.2.3. Data Processing

Pressure values measured on the model surface and in the wake are the basis of determining the integral forces acting on the airfoil. The pressure distribution around the airfoil can be used to evaluate the airfoil's lift and pitching moment by integrating pressure coefficients around the surface of the wing. This is accomplished numerically using the trapezoid rule.

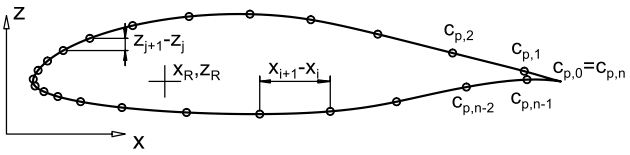

FIG 8. Airfoil contour with pressure taps

The integration in the model fixed coordinate system provides the normal and longitudinal force coefficient:

$$c_z = \sum_{i=0}^{n-1} \frac{\left(c_{p,i+1} + c_{p,i}\right)}{2} \frac{\left(x_{i+1} - x_i\right)}{c}$$
$$c_x = -\sum_{i=0}^{n-1} \frac{\left(c_{p,i+1} + c_{p,i}\right)}{2} \frac{\left(z_{i+1} - z_i\right)}{c} \quad (8)$$

In cases of blunt trailing edges, such as split flaps, the pressure is constant over the respective contour element due to flow separation. Transformation into streamwise coordinates yields:

$$c_L = c_z \cos\alpha - c_x \sin\alpha$$
$$c_{D,p} = c_x \cos\alpha + c_z \sin\alpha \quad (9)$$

The pitching moment around the reference point x_R,z_R (FIG 8) is obtained by:

$$c_M = \sum_{i=0}^{n-1} \frac{\left(c_{p,i+1} + c_{p,i}\right)}{2} \frac{\left(x_i + x_{i+1} - 2x_R\right)\left(x_{i+1} - x_i\right)}{2c^2} + \sum_{i=0}^{n-1} \frac{\left(c_{p,i+1} + c_{p,i}\right)}{2} \frac{\left(z_i + z_{i+1} - 2z_R\right)\left(z_{i+1} - z_i\right)}{2c^2} \quad (10)$$

The total airfoil drag is determined from the integrated total pressure loss in the wake:

$$c_{D,ges} = \sum_{i=0}^{n-2} \left(\sqrt{c_{p,i}} - c_{p,i} + \sqrt{c_{p,i+1}} - c_{p,i+1}\right) \frac{z_{i+1} - z_i}{c} \quad (11)$$

To obtain curves of lift versus effective angle of attack, a correction of the test section blockage must be applied. In an open test section, the flow is more strongly deflected by the lift than in a two-dimensional case. Thus, the airfoil's effective angle of attack is lower than the geometric angle of the model (FIG 9).

The corrector value is proportional to the lift with a factor that is determined by the model's chord length and the test section dimensions. This factor can be obtained by either a lifting line calculation or evaluation of the pressure distribution. As long as no flow separation occurs, the pressure drag of an airfoil is two to three orders of magnitude lower than its lift. Therefore, the resulting pressure force can be assumed to be perpendicular to the effective flow direction.

$$\alpha_{EFF} = -\arcsin\left(\frac{c_x}{c_z}\right) \quad (12)$$

This factor is to be determined for a plain airfoil in the linear regime, where $c_{D,p}$ is low, but it is valid for all other cases. This way, a corrector value of -4.35° was determined.

$$\frac{\alpha_{EFF} - \alpha}{c_L} \approx -4.35° \quad (13)$$

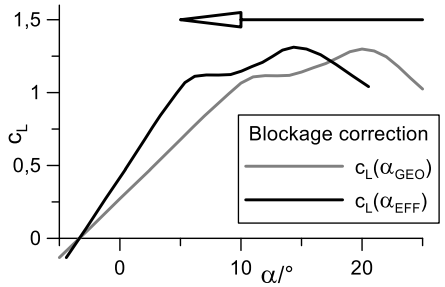

FIG 9. Effect of test section blockage and its correction on the lift curve

3. PLAIN AIRFOIL DESIGN

3.1. Basic Airfoil Selection

The i-2 operates in a Reynolds number range where a classical laminar airfoil functions. For steady, straight and level flight, Re is a function of the lift coefficient. Wing loading, chord length and altitude result in a reference Reynolds number:

$$\mathrm{Re} = \frac{u_\infty c \rho}{\mu};\ u_\infty = \sqrt{\frac{2mg}{\rho S c_L}} \quad (14)$$

$$\mathrm{Re}\sqrt{c_L} = \mathrm{Re}\left(c_L = 1\right) = \frac{c}{\mu}\sqrt{\frac{2mg\rho}{S}} \quad (15)$$

The Reynolds number at $c_L = 1$ is $3.54 \cdot 10^6$ at cruise altitude and $4.02 \cdot 10^6$ at sea level, representing the landing

condition. The flow is assumed to be incompressible in all cases. Several laminar airfoils were evaluated using XFOIL in the constant lift mode to find a proper base airfoil to modify. Three examples are considered here (FIG 10, 11):

The HQ-42 is an airfoil designed for small, powered aircraft and had initially been proposed by the project leader. It has a relative thickness of 15%.

The E-603 is primarily used in basic training gliders, such as the Grob Twin Astir. It has pleasant stall characteristics and provides much internal space due to its relative thickness of 19%.

The FX-73 is an airfoil for higher performance gliders, such as the DG-500. Thus, better performance can be expected, and it is still comparatively thick (17%).

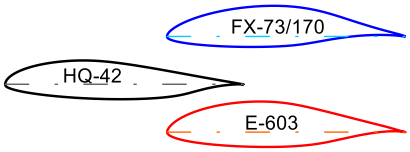

FIG 10. Shapes of the considered airfoil examples

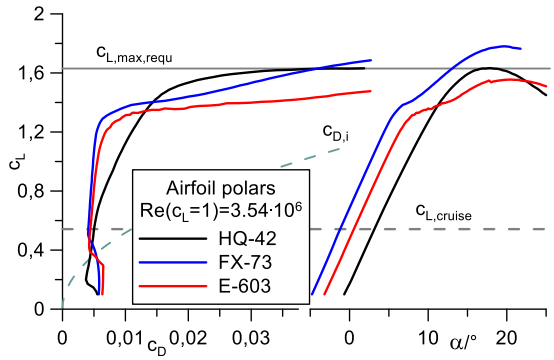

FIG 11. Lift curves and drag polars of the considered airfoil examples (XFOIL-calculation)

Because of its weak camber, the HQ-42's laminar bucket reaches low c_L values with its optimum close to the lower end, which is far below $c_{L,cruise}$ of the aircraft. $c_{L,max}$ is also not satisfied as it just touches the requirement in one point. Moreover, the zero-lift angle of attack of -1.5° requires high incidence of the wing in respect to the fuselage, meaning the wing will need significantly more vertical space under the cockpit than its thickness.

The E-603 provides better performance at the desired $c_{L,cruise}$, but it does not satisfy the $c_{L,max}$ requirement at all. The lift increase beyond the upper edge of the laminar bucket is comparatively small.

The FX-73 theoretically fulfils the lift coefficient criteria and has a lower $c_{D,cruise}$ than all competitors. The shape of the c_L-α-curve also promises pleasant stall characteristics. Ultimately, it was chosen as the starting point for the design of the final airfoil. Picking an airfoil known from gliders rather than one specifically designed for powered aircraft is reasonable because of the more demanding aerodynamic performance requirements due to the lower power density of the alternative propulsion system.

3.2. Optimization

Modifications were applied to the camber to move the lower end of the laminar bucket downward, maintaining laminar flow at cruise speed also for lower wing loading. A camber reduction by 20% (FIG 12) lead to shift of the laminar bucket of $\Delta c_L(c_{D,min})$=-0.1; meanwhile $c_{L,max}$ seems still sufficient (FIG 13).

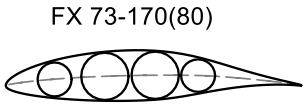

FIG 12. FX-73 with camber reduced by 20% and an arrangement of hydrogen tubes inside

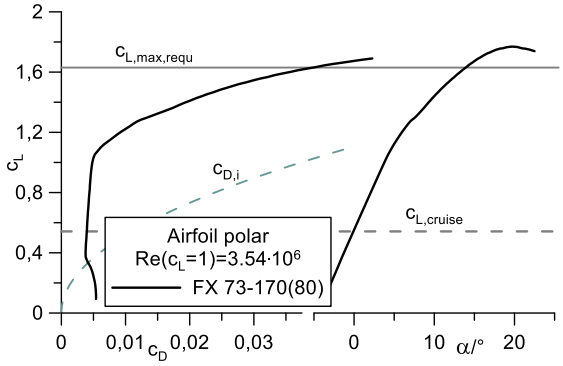

FIG 13. Lift curve and drag polar of FX-73 with 20% reduced camber (XFOIL-calculation, cruise-condition)

Thickness distributions were also modified to create additional space inside the wing, particularly for the most forward and rearward tube. One observes pressure distributions with two suction peaks that cause the boundary layer transition to jump from peak to peak at distinct angles of attack. Thus, the polar does not leave the laminar bucket at once but in two steps (FIG 14). This is likely not critical as these steps occur at c_L where the induced drag is much higher, but these modifications were ultimately discarded because of additional space limitations in the chordwise direction and the need to accommodate other system components.

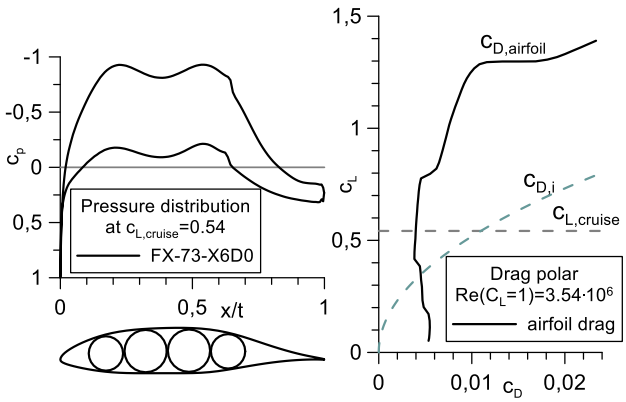

FIG 14. Effect of a modified thickness distribution on internal space (esp. forward and rearward tube), pressure distribution and drag polar

3.3. Experimental Validation

XFOIL tends to deliver optimistic results in both drag and maximum lift, so an experimental validation in the wind tunnel is necessary. As the wind tunnel is not capable of providing free flight Reynolds numbers, the XFOIL data is still useful to extrapolate from wind tunnel to free flight conditions.

Wind tunnel measurements were conducted with the model described in section 2. For the plain airfoil, the Reynolds number was varied from $0.75 \cdot 10^6$ to $1.44 \cdot 10^6$. The geometric angle of attack was swept from α=-5° to 25° for all cases. The effective angle of attack range differs from the geometric angle of attack due to blockage correction.

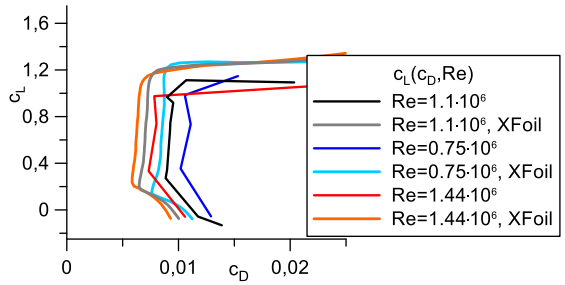

FIG 15. Experimental drag polars of the plain airfoil for the covered Reynolds numbers compared to XFOIL results

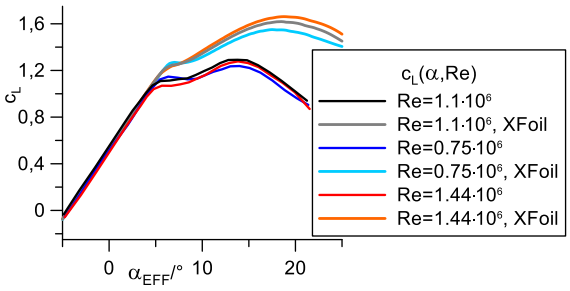

FIG 16. Experimental lift curves of the plain airfoil for the covered Reynolds numbers compared to XFOIL results

As expected, the laminar bucket is smaller and the viscous drag higher than predicted by XFOIL (FIG 16). The effect of Re on c_D is in the same order of magnitude as predicted. Furthermore, $c_{L,max}$ is significantly lower than in the XFOIL calculation (FIG 17). Combined with the reduced width of the laminar bucket this clearly indicates the necessity of high lift devices for the aircraft APUS i-2.

4. HIGH LIFT DEVICES

4.1. Split Flap Design

The maximum lift coefficient, $c_{L,max}$, for the i-2 aircraft must be a minimum of 1.63. A rigid airfoil does not provide the maximum lift required in slow flight and laminar flow under cruise conditions, so high lift devices are necessary for the design. Part of the decision of which high lift device to use involves ease of manufacturing. The design ultimately incorporates split flaps on the outer part of the rectangular section between the nacelles and the ailerons. The flap hinge is positioned at 80% of the chord length on the pressure side (FIG 17).

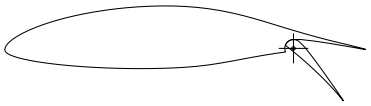

FIG 17. Diagram of airfoil with split flap

Unlike plain flaps, where the entire trailing edge pivots, split flaps only deflect on the pressure side and have a continuous contour on the suction side. This means the boundary layer is less susceptible to separation at high flap angles to achieve maximum lift (FIG 18). Moreover, there is no gap between the main airfoil body and the split flap on the suction side, as is present on a plain flap. Thus, the boundary layer is less disturbed, making the split flap favourable for cruise. However, for smaller deflections, the split flap's blunt trailing edge tends to create additional drag.

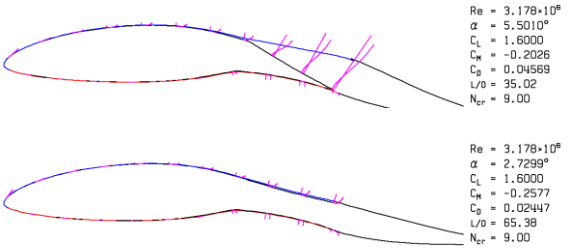

FIG 18. XFOIL-calculated flow over an airfoil with plain flap (top) and split flap (bottom); the displacement thickness (blue) and velocity profiles (violet) indicate a large flow separation on the suction side at the hinge of the plain flap, meanwhile with the split flap, the flow remains attached to the continuous contour.

It should be stated that XFOIL's capability to handle split flaps was not taken for granted. However, the solution converges in most scenarios, making XFOIL a promising tool for theoretical estimations. Only with increased flap deflection does the blunt trailing edge cause the viscous solution to fail.

The XFOIL-predicted lift increase produced by the split flap is quite promising. Maximum lift coefficients exceed values of 2.5 (FIG 19).

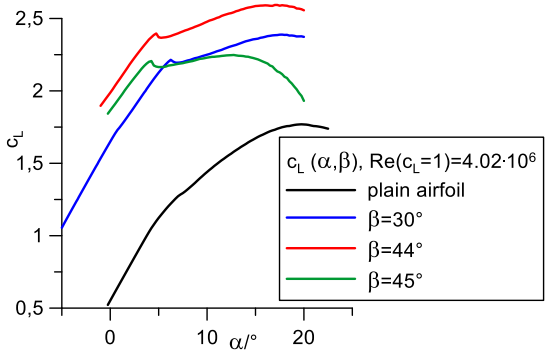

FIG 19. XFOIL-calculated lift curves for the airfoil with varying split flap deflection β under landing conditions

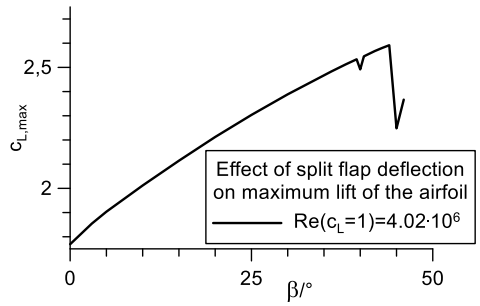

FIG 20. XFOIL-calculated maximum lift depending on split flap deflection β under landing conditions

A sudden breakdown can be registered when the flap angle reaches a threshold of 45° (FIG 20) together with the occurrence of errors in the viscous solution. Additionally, the 2D tool cannot cover three-dimensional flow separation, so the wind tunnel test is necessary for the split flap airfoil.

4.2. Experimental Validation

All measurement concerning the split flap were conducted with the same wind speed resulting in $Re=1.1\cdot10^6$. Flap angles up to 75° were investigated. The geometric angle of attack was swept from α=-5° to 25° again.

The shape of the pressure distributions is in good agreement with the XFOIL-prediction for respective lift coefficients (FIG 21). Besides a certain difference in the nose-region one may notice the lower pressure at trailing edge. This deviation is a plausible explanation for the significantly higher drag observed in the experiment as described later (FIG 26).

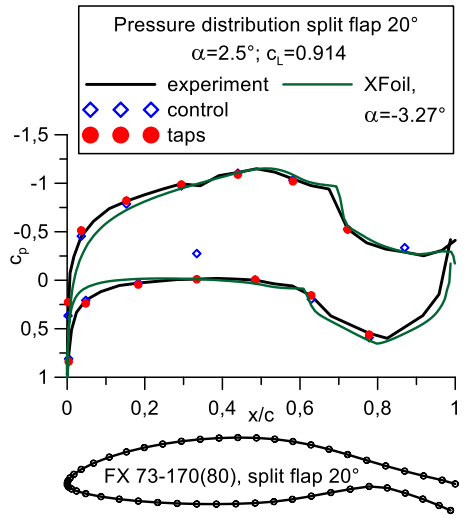

FIG 21. Experimental pressure distribution around the airfoil with split flap deflected by 20° compared to XFOIL-calculation for the same c_L

Two measuring campaigns were conducted to gather pressure distributions around the real airfoil model and produce lift curves. The first campaign in 2021 gathered pressure data for lower flap deflections up to 50° (FIG 22), while the second campaign in 2022 handled high flap deflections up to 75° (FIG 23). A small misalignment in angle of attack between the first and second test campaigns makes direct comparison of the lift curves not plausible, so they are presented in separate diagrams.

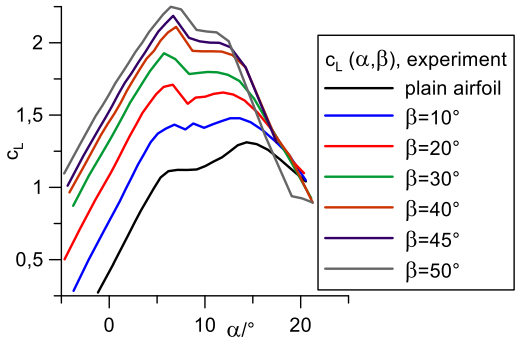

FIG 22. Lift curves produced in the 2021 measuring campaign with flap angles up to 50 degrees.

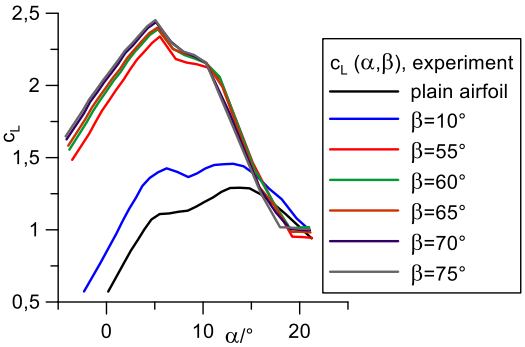

FIG 23. Lift curves produced in the 2022 measuring campaign with flap angles of 0, 10, and 55 to 75 degrees

The experimental lift coefficients at all angles of attack tend to be lower than the XFOIL prediction. Especially the further increase beyond the laminar bucket vanishes with increasing flap angle and changes to a plateau with negative slope more and more (FIG 22, 23).

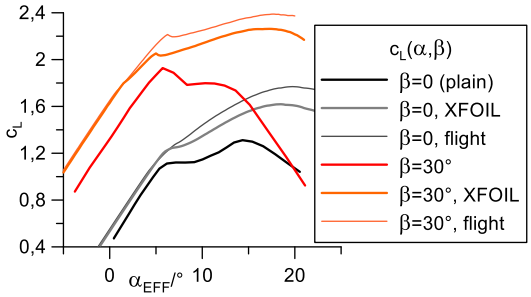

FIG 24. Experimental lift curve at flap angles of 0° and 30° compared to theoretical lift curves for wind tunnel and free flight conditions

The effect of the split flap on zero lift angle of attack is significantly lower than predicted (FIG 24). It was found to be 33% lower in experiment (-0.2) than in XFOIL (-0.3). XFOIL's overprediction in maximum lift is the same for the plain airfoil and the considered range of split flap angles. The absolute maximum achieved in the wind tunnel is equal to the prediction but occurs at much higher flap angles. While XFOIL predicts a $c_{L,max}$ breakdown at 45°, the experimental data continues an increasing trend with a

gradual saturation at higher flap angles (FIG 25).

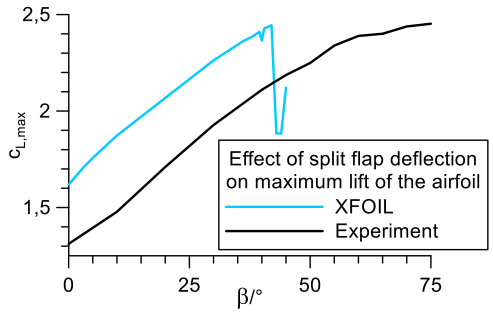

FIG 25. Increase in maximum lift coefficient achieved with the split flap in experiment and XFOIL calculation (wind tunnel conditions)

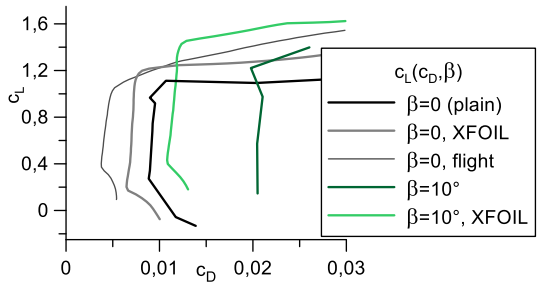

FIG 26. Experimental drag polars at flap angles of 0° and 10° compared to theoretical polars for wind tunnel and free flight conditions

The drag polar shows a substantial difference between theoretical and experimental results (FIG 26). The separated flow properties downstream of the trailing edge and inside the open flap are beyond the capabilities of the model XFOIL is based on, but airfoil drag is still not the dominant parameter in flight regimes where flaps are used.

One lesson learned from the measurements with the experimental setup described is a lack of stiffness within the electro-mechanical system that led to lower flap angles than commanded while under aerodynamic load. In the 2021 campaign, this problem was solved by continuous visual monitoring during the test. As flap angles above 50° exceed the range of the electro-mechanical system anyway, a physical wedge held the flap open in all cases presented here for the 2022 campaign.

4.3. Maximum Lift of the Entire Wing

Due to the continuous circulation distribution, the actual non-elliptical wing will not reach the airfoil's $c_{L,max}$ over its entire span. Steps in zero lift angle caused by flap deflection result in additional strong lift gradients at the flap tips. Airfoil lift curves gained from wind tunnel measurements were fed into the in-house lifting line algorithm to calculate the maximum lift of the actual wing. The maximum lift has been determined for the clean wing, the wing with flaps between the nacelles and the ailerons as well as with a continuous flap from aileron to aileron (FIG 27).

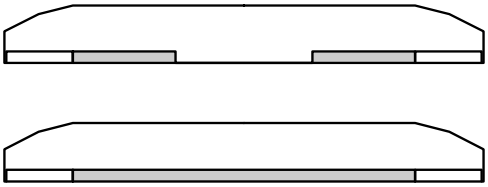

FIG 27. Planform views of the investigated flap configurations; top: flaps only between nacelles and ailerons on both sides (small); bottom: continuous flap from aileron to aileron (large).

Descending airfoil lift curves at post stall can cause troubles concerning numeric instability. The solution starts to oscillate between effective angles of attack before and after maximum lift due to the finite trailing vortices, which causes a breakdown of the lift (FIG 28). In this respect, the results can be called conservative concerning the effect of a continuous lift distribution on maximum lift. The problem of oscillating lift distributions has been observed by several authors before, among them John D. Anderson [10].

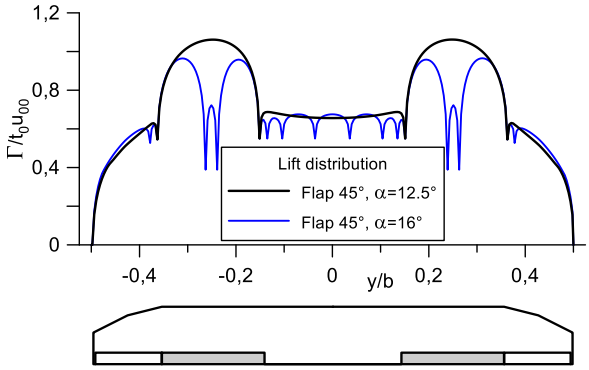

FIG 28. Lift distribution with small flap at 45° deflection close to $c_{L,max}$; meanwhile still reasonably looking at α=12.5°, the calculation collapses at α=16°.

At a flap angle of 75°, the required maximum lift coefficient of $c_{L,max}=1.63$ could be reached with flaps only between the nacelles and ailerons (FIG 29). The shape of the lift distribution at maximum lift almost doubles the k-factor for induced drag compared to the clean wing.

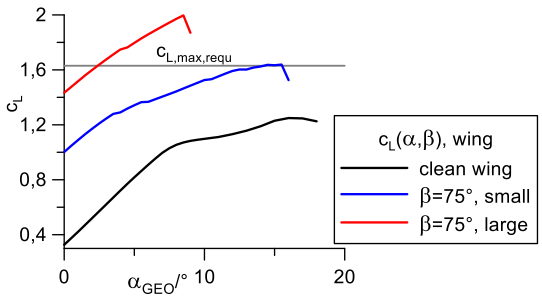

FIG 29. Lift curves for the finite wing and maximum flap deflection for small flaps (nacelles to ailerons) and large flaps (aileron to aileron)

5. ROLL MANOEUVRABILITY / AILERONS

Only the small tapered outer part of the wing is equipped with ailerons, making rolling agility a concern. Lifting line

calculations were conducted to determine the initial roll moment as well as the steady roll rate (FIG 31) for several configurations including flap settings. A slightly differential deflection was applied to the ailerons. The yawing moment was also examined for all cases.

The ailerons have constant chord, so the relative hinge position changes from 80% inboard to 64% outboard (FIG 30). The range of aileron deflection is from -25° to +15°. XFOIL was used to determine the shift in zero-lift angle of attack caused by aileron deflection for varying hinge positions.

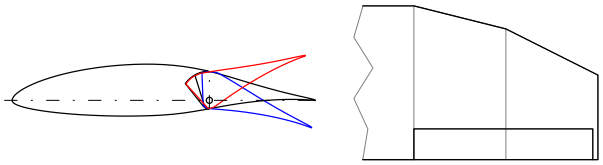

FIG 30. Aileron geometry and maximum deflection

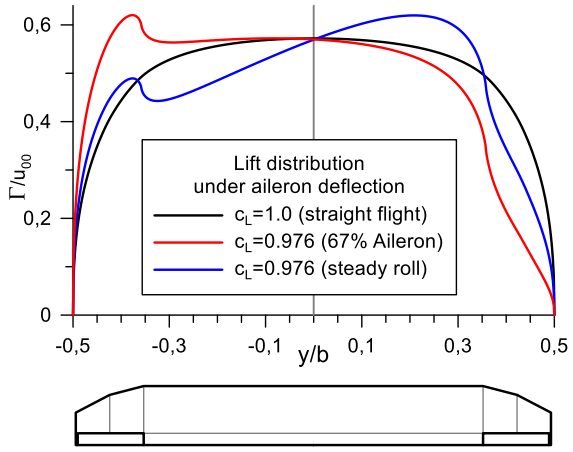

FIG 31. Lift distributions for pure aileron deflection and a steady rolling manoeuvre

The calculations indicate a sufficient controllability of the aircraft about the roll axis. The adverse yawing moment is only small or even a bit favourable for steady roll manoeuvres (TAB 2, 3).

TAB 2. Aileron effectiveness for straight flight in cruise and landing configuration, $y_{c,L}/b$ and $y_{c,D}/b$ are the spanwise acting points of the resulting lift and induced drag.

c_L, airspeed	± β	$y_{c,L}/b$	$y_{c,D}/b$
0.976, 44 m/s	-15.55°/ +11.11°	0.0533	0.1628
1.447, 32 m/s	-25°/ +15°	0.053	0.0591

TAB 3. Aileron effectiveness for steady roll in cruise and landing condition, $y_{c,D}/b$ is the spanwise acting point of the resulting induced drag, ω_X is the roll rate

c_L, airspeed	± β	$y_{c,D}/b$	ω_X
0.975, 44 m/s	-15.55°/ +11.11°	0.0143	34°/s
1.446, 32 m/s	-25°/ +15°	-0.0461	35°/s

6. WING TIP DEVICES

As stated before, induced drag is a dominant aerodynamic resistance on the given wing, even under cruise conditions. Thus, further efforts are worthwhile to optimize wing tip design. Span loading is the most relevant parameter for induced drag, so increasing wingspan is the most promising method of reducing induced drag. Additionally, lift distribution can be optimized, and vertical surfaces like winglets can increase wing efficiency. Athena Vortex Lattice was used for detailed calculations on modifications to the wing tips.

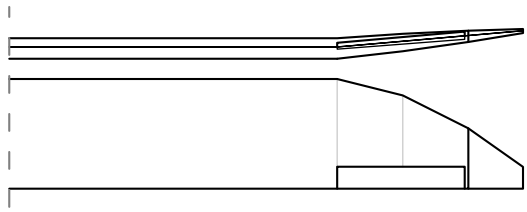

FIG 32. Half span wing geometry with tip extensions

To reduce induced drag, wing tip extensions have been applied by adding another trapezium to each side, increasing the wingspan by 1.5m, or 12%; this also creates a more elliptically shaped planform (FIG 32). AVL calculates an induced drag reduction of 21% due to the reduced span loading a slightly improved lift distribution (FIG 33). Considering Reynolds number, viscous drag may increase by up to 10%. Total wing drag should be reduced by 18% under cruise conditions. A slight increase of the lifting surface by 5% should help to improve flight performance at lower speeds.

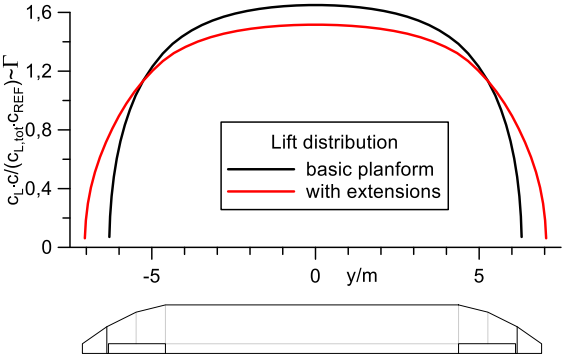

FIG 33. Effect of wing tip extensions on the lift distribution for the same total lift

The effect of winglets, including single upward pointing and split winglets, has also been investigated. Compared to the wing tip extensions, the effect on induced drag is lower but stronger in relation to the extra wetted surface. However, Reynolds numbers are even lower then. When using winglets another airfoil should be considered for them.

7. CONCLUSIONS AND OUTLOOK

This paper presents a wing design solution that meets or exceeds the requirements for the APUS i-2 hydrogen-powered aircraft. The wing houses sufficient internal space to store hydrogen fuel while also exhibiting low drag characteristics in cruise conditions. A split flap design on

the wing produces enough additional lift to meet stall speed requirements, and the cruise and maximum lift coefficient requirements were met. Additionally, XFOIL calculations demonstrated satisfactory aileron capability on the wing, and wingtip devices are shown to potentially reduce induced drag by up to 21%. Overall, the development and design of the i-2 aircraft's wing provides a basis for structural wing integration and technology development for alternative energy aircraft. Addressing the logistics of the full wing's physical construction is planned as the maiden flight of the concept aircraft approaches.

8. NOMENCLATURE

TAB 4. List of variables used

Symbol	Units	Description
b	m	Wingspan
c	m	Chord length
c_D	-	Drag coefficient
$c_{D,i}$	-	Induced drag coefficient
$c_{D,p}$	-	Pressure drag coefficient
c_L	-	Lift coefficient
$c_{L,max}$	-	Maximum lift coefficient
$c_{L,max,requ}$	-	Required max. lift coefficient
c_M	-	Pitching moment coefficient
c_p	-	Pressure coefficient
k	-	Damping coefficient
g	m/s^2	Gravitational acceleration
L	N	Lift force
Ma	-	Mach number
m	kg	Mass
$MTOW$	kg	Maximum take-off weight
Re	-	Reynolds number
S	m^2	Lifting surface area
u, v, w	m/s	Velocity components in x, y, z
u_∞	m/s	Airspeed
w_i	m/s	Induced vertical velocity
x, y, z	m	Cartesian coordinates
α	°	Angle of attack
α_0	°	Zero lift angle of attack
α_{EFF}	°	Effective angle of attack
α_i	°	Induced angle of attack
α_{GEO}	°	Geometric angle of attack
β	°	Flap / aileron deflection angle
Γ	m^2/s	Vortex strength
μ	Pa·s	Dynamic viscosity
ρ	kg/m^3	Air density
ω	°/s	Roll rate

9. REFERENCES

[1] https://ec.europa.eu/clima/eu-action/european-green-deal/delivering-european-green-deal/aviation-and-eu-ets_en, called on 09.09.2022.

[2] Kreimeier, M., Stumpf, E: "Benefit evaluation of hybrid electric propulsion concepts for CS-23 aircraft," CEAS Aeronautical Journal 8, 691–704 (2017). doi: 10.1007/s13272-017-0269-9.

[3] Gao, Y., Jausseme, C. Huang, Z., Yang, T.: "Hydrogen-Powered Aircraft: Hydrogen–electric hybrid propulsion for aviation," IEEE Electrification Magazine, vol. 10, no. 2, pp. 17-26, June 2022, doi: 10.1109/MELE.2022.3165725.

[4] Kallo, J.: "Emission free flight with Hydrogen: dream or reality?" Systainable Aircraft Symposium, 6.-7. Mai 2016, San Francisco, USA, https://elib.dlr.de/110733/.

[5] Arat, H. T., Sürer, M.G., Gökpinar, S., Aydin, K.: "Conceptual design analysis for a lightweight aircraft with a fuel cell hybrid propulsion system, Energy Sources, Part A: Recovery, Utilization, and Environmental Effects," 2020, doi: 10.1080/15567036.2020.1773966

[6] Morgadoa, J., Vizinhob, R., Silvestrea, M.A.R., Páscoab, J.C.: "XFOIL vs CFD performance predictions for high lift low Reynolds number airfoils," Aerospace Science and Technology, vol 52, pp 207-214, May 2016, doi: 10.1016/j.ast.2016.02.031.

[7] Ting, E., Reynolds, K. W., Nguyen, N. T., Totah, J.: "Aerodynamic Analysis of the Truss-Braced Wing Aircraft Using Vortex-Lattice Superposition Approach," AIAA 2014-2597, doi: 10.2514/6.2014-2597.

[8] Drela, M.: "XFOIL: An Analysis and Design System for Low Reynolds Number Airfoils," In: Mueller, T.J. (eds) Low Reynolds Number Aerodynamics. Lecture Notes in Engineering, vol 54., pp. 1-12, 1989.

[9] Drela, M., Youngren, H.: "MIT AVL User Primer – AVL 3.36," 2017.

[10] Anderson, J. D., Corda, S., Wie, D. M. V.: "Numerical Lifting Line Theory Applied to Drooped Leading-Edge Wings Below and Above Stall," Journal of Aircraft, Vol. 17, 1980, pp. 898–904.

10. ACKNOWLEDGMENT

The authors would like to thank all the partners for the outstanding cooperation within the research project HydroTube, namely APUS GmbH, COTESA GmbH, KVB gGmbH and the Chair of Aircraft Systems at TU Dresden.

The HydroTube project is part of the Aerospace Research Program LuFo VI that is funded by the Federal Ministry for Economic Affairs and Climate Action, BMWK.